



Thermal management of cylindrical batteries investigated using wind tunnel testing and computational fluid dynamics simulation



Xuesong Li^a, Fan He^b, Lin Ma^{a,b,*}

^a Department of Aerospace and Ocean Engineering, Virginia Tech, Blacksburg, VA 24061, USA

^b Department of Mechanical Engineering, Virginia Tech, Blacksburg, VA 24061, USA

HIGHLIGHTS

- CFD model has been developed to simulate the cooling of multiple battery cells.
- Direct comparison between CFD simulations and experimental data.
- A reduced-order model is developed to predict the maximum battery cell temperature.

ARTICLE INFO

Article history:

Received 20 February 2013

Accepted 12 April 2013

Available online 22 April 2013

Keywords:

Battery thermal management

CFD modeling

Wind tunnel testing

Reduced-order model

ABSTRACT

This work studied the thermal management of lithium ion batteries both numerically and experimentally. Numerically, a two dimensional CFD (computational fluid dynamics) model has been developed to perform detailed simulations of the thermal management issues within a battery pack cooled by air. Experimentally, systematic tests were performed to provide datasets to validate the CFD model. The main components in the experimental facility included a multi-cell battery pack and a wind tunnel. The wind tunnel facility generated well-controlled cooling air flow with velocity up to 30 m s^{-1} (~ 67 miles per hour). So that the study can be performed under flow conditions directly relevant to practice. The major contributions from this combined numerical-experimental study are threefold. First, the CFD model has been shown to capture the dynamics of the cooling of battery modules consisting of multiple battery cells, including temperature non-uniformity among cells. Second, the CFD simulations have been compared directly against experimental data to quantify the accuracy and validity of the CFD models. Third, based on the validated CFD models, a reduced-order model is developed to predict the maximum cell temperature in the battery module. The accuracy and simplicity of the reduced-order model makes it promising for *in situ* monitoring and control purposes.

© 2013 Elsevier B.V. All rights reserved.

1. Introduction

In the past few years, secondary lithium ion batteries have been widely employed by electric vehicles (EVs) and hybrid electric vehicles (HEVs). The use of lithium ion batteries is favored because of their high-voltage, low self-discharge rate, and their high energy density [1]. However, the performance of lithium ion batteries is significantly restricted by their long term stability and safety characteristics [2]. The temperature of lithium ion batteries is usually limited within the range of 0–40 °C, while the ambient

temperature under which the vehicles operate can be well beyond this range. Overheating or uneven cell temperature distribution will cause cell degradation and cell failure. Cell degradation leads to considerable loss of voltage and electric capacity, and cell failure leads to thermal runaway or even fire hazard [3]. Therefore, the thermal management of lithium ion batteries is critical for considerations of both vehicle performance and vehicle safety.

As a result, the investigation of battery thermal management has attracted considerable research and development efforts. Past efforts relevant to this work can be broadly divided into two categories. The first category of efforts focused on the modeling of the governing electro-thermal processes in batteries. Notable examples of the research work in this category include the models based on first-principles to simulate the state of charge (SOC) of lithium ion batteries [4–6], a critical parameter that influences the performance and heat generation rate of lithium ion batteries. Advanced

* Corresponding author. Laser Diagnostic Lab., Room 215 Randolph Hall, Department of Aerospace and Ocean Engineering, Virginia Tech, Blacksburg, VA 24061, USA. Tel.: +1 (540) 231 2249; fax: +1 (540) 231 9632.

E-mail address: linma@vt.edu (L. Ma).

experimental techniques such as neutron imaging are being employed to make *in situ* measurements of lithium concentration to validate these models. Equipped with a fundamental understanding of the governing processes, other models are being developed to simulate other aspects of battery operations, including the heat generation in battery cells under different operation conditions and battery geometries using one-dimensional (1D) [7–9], 2D, and 3D models [10–12]. The second category of efforts focused on investigating methods to effectively manage the heat dissipated from the batteries during operation, and various thermal management models and techniques have been proposed [13–15]. These techniques attempted to optimize the thermal management of batteries by adjusting one or more of these following variables: cooling flow pattern [16], the cooling medium [17–20], and the control strategy [21,22]. The goals of these techniques are to maximize the cooling effectiveness and/or to minimize the temperature non-uniformity and fluctuations.

Based on these past efforts, this current work focuses on the development and validation of thermal management models for battery modules. The uniqueness of this work lies in the combined use of CFD (computational fluid dynamics) simulations and wind tunnel testing, so that the simulations can be validated against experimental data under air flow velocities which are both well-controlled and directly relevant to practical conditions. In contrast, past work predominately relied on modeling and numerical simulation with limited experimental validation [16–22]. This work developed an experimental facility that is capable of testing various battery packing geometries, charging and discharging currents, and various cooling air flow velocities. The cooling air flow is generated by an open jet wind tunnel, with freestream velocity controllable in the range of 0.5 m s^{-1} to 30 m s^{-1} (corresponding to ~ 1.1 to 67 miles per hour), encompassing conditions expected in most practical applications.

The major contributions of this work are threefold. First, a high-fidelity CFD model has been developed to simulate detailed dynamics of the cooling of battery modules consisting of multiple cylindrical Li-ion ($\text{LiMn}_2\text{O}_4/\text{C}$) battery cells, including cell-to-cell temperature variation. Second, the CFD simulations have been compared directly against experimental data, quantifying the accuracy and validity of the CFD models. Third, based on the validated CFD models, a reduced-order model is developed to predict the maximum cell temperature in the battery module. The accuracy and simplicity of the reduced-order model makes it promising for *in situ* control purposes.

The rest of this paper is organized as the following. Section 2 introduces the CFD model used in this study, and comments on the accuracy of the CFD simulation relative to results archived in past literature. Section 3 described the experimental arrangement used in this work. Section 4 focuses on reporting and discussing the direct comparison between the CFD model and the experimental results. Section 5 introduces a reduced-order model to predict the maximum cell temperature in the battery module. Finally, Section 6 summarizes and concludes the paper.

2. CFD model

Fig. 1 provides a schematic illustration of the thermal management problem that this work targets. The cooling air enters from the left, flows across the Li-ion cells, and exit from the right. Each Li-ion ($\text{LiMn}_2\text{O}_4/\text{C}$) battery cell is presented as a cylinder as shown in panel (a) of Fig. 1. Each cell has a diameter $D = 42.4 \text{ mm}$ and a height $H = 62.5 \text{ mm}$ (not shown in Fig. 1). An in-line arrangement was considered in this work, though other configurations can be studied with minimal modification of our existing CFD model and experimental facility. The in-line arrangement is

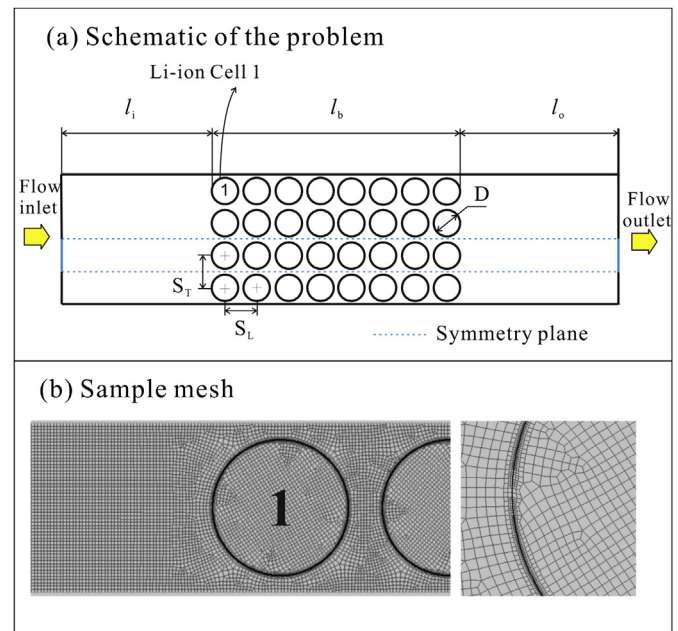


Fig. 1. Schematic of problem definition (Panel a) and sample mesh of and around cell 1 at $U = 5 \text{ m s}^{-1}$ (Panel b).

characterized by the transverse pitch (S_t) and the longitudinal pitch (S_L), which are both set to be 53 mm in this work. Other parameters used in the model include the distance from the inlet of the air flow to the front edge of the first column of batteries (l_i), the overall length of the battery pack (l_b), and the distance from the rear edge of the last column of batteries to the outlet of the air flow (l_o). This model empirically set $l_i = l_o = 323.3 \text{ mm}$, and l_b was calculated to be 413.4 mm with eight columns of battery cells.

This work used the ANSYS/FLUENT 14.0 CFD package to model the thermal management problem as a 2D conjugate heat transfer problem, with the rates of heat release dependent on cell temperatures. The model considered a fluid zone and solid zone to model the cooling air and batteries, respectively. Uniform quadrilateral meshing method was applied to both the liquid and solid zones, as shown in Panel (b) of Fig. 1 at an air flow velocity of $U = 5 \text{ m s}^{-1}$. The adapted boundary layer is shown in the enlarged figure shown on the right in Panel (b), illustrating that the grids near the fluid–solid interface is significantly finer to capture the boundary layer. A user defined function (UDF) was created and applied to model the variable heat release rate as a function of cell temperature. The Reynolds stress and renormalization group turbulent model (i.e., the $k-\varepsilon$ model) was employed with enhancement wall treatment. The boundary conditions used include the velocity inlet, pressure outlet, and no-slip condition at walls and battery surfaces. The Unsteady Reynolds-Averaged Navier–Stokes (URANS) equations were solved by FLUENT to obtain the evolution of temperature distribution, and the Reynolds-Averaged Navier–Stokes (RANS) equations solved to obtain the steady-state temperature distribution.

Meshing is an important aspect of the CFD modeling. In this work, the size of the grids was chosen in such a way that the resultant temperatures are independent of the grid size. Inflation option was used to model the flow boundary layers and to keep the wall y^+ number within an acceptable range. The y^+ number, defined below in Eq. (1), was kept around 1.0 in this work as required by the enhancement wall treatment:

$$y^+ \equiv \frac{y}{\nu} \sqrt{\frac{\tau_w}{\rho_f}} \quad (1)$$

In Eq. (1), ν is the local kinematic viscosity, y the distance to the nearest wall (i.e., the thickness of the boundary layer grids here), τ_w the wall shear stress, and ρ_f the density of the fluid. For $U = 5 \text{ m s}^{-1}$ case, our meshing method resulted in a total number of 442,133 grids for the 32 batteries cells as shown in Panel (a) of Fig. 1. For such a case, the computational cost was about 4–6 h using a Dell workstation with six processing cores from two quad-core Xeon 3.20 GHz CPUs.

To verify our CFD model, we calculated the overall heat transfer coefficient (h) using our model, and compared the results to those archived in the literature [23]. For comparison purpose, we selected a region contained 8 cells in a row as shown in Panel (a) of Fig. 1. Different freestream velocities U ranging from 0.02 m s^{-1} to 20 m s^{-1} were tested to cover the range of Reynolds number (Re) where past data exist. Here, the Re number is customarily defined based on the maximum velocity (U_{\max}) as:

$$Re = \frac{\rho_f U_{\max} D}{\mu_f} \quad \text{where} \quad U_{\max} = \frac{S_T}{S_T - D} U \quad (2)$$

where μ_f is the dynamic viscosity of the fluid. With U ranging from 0.02 m s^{-1} to 20 m s^{-1} , the Re number ranges from 266 to 266,000, covering the laminar flow regime to fully developed turbulent regime. To match the conditions in Ref. [23], the upper wall and lower wall were set to be symmetric boundaries. Again, the model adjusted the boundary layer grid thickness so that the wall y^+ number was kept around 1.0 across all Re numbers.

Fig. 2 compares Nusselt number (Nu) obtained by the CFD model against past experiments and empirically correlations published in Ref. [23]. Here, the Nu is defined as:

$$Nu = \frac{hD}{k_f} \quad (3)$$

where k_f is the heat conductivity of air, and h the overall heat transfer coefficient. Here, h is defined as shown below using a log-mean temperature difference (LMTD) [24]:

$$h = \frac{\dot{M}_f C_f (T_{f,o} - T_{f,i})}{n\pi D H \cdot T_{\text{LMTD}}} \quad \text{and} \quad T_{\text{LMTD}} = \frac{(T_8 - T_{f,o}) - (T_1 - T_{f,i})}{\ln \left(\frac{T_8 - T_{f,o}}{T_1 - T_{f,i}} \right)} \quad (4)$$

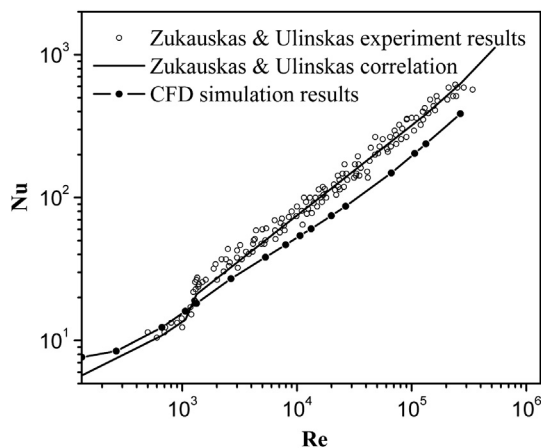


Fig. 2. Comparison of Nu number obtained by CFD model against past experiments and empirically correlation.

where \dot{M}_f is the mass flow rate of air, $T_{f,o}$ is the average temperature of air at the outlet, $T_{f,i}$ is the average temperature of air at the inlet (25°C in this research), n is the number of cells in a row ($n = 8$ for the results shown in Fig. 2), and T_1 and T_8 are the average temperature of the first cell and last cell in the row, respectively [16].

According to Ref. [23], the Nu number can be correlated to Re number as defined in Eq. (2), the Prandtl number of the fluid under the inlet conditions (Pr) and near the wall of the batteries (Pr_w), and the relative traverse and longitudinal pitch (defined as $a = S_T/D$ and $b = S_L/D$). The results shown in Fig. 2 were obtained with $a = b = 1.25$, and the correlations developed in Ref. [23] reduce to Eq. (5) under these conditions:

$$Nu = 0.51 Re^{0.5} Pr^{0.36} (Pr/Pr_w)^{0.25}, \quad \text{when } 10^2 < Re < 10^3$$

$$Nu = 0.27 Re^{0.63} Pr^{0.36} (Pr/Pr_w)^{0.25}, \quad \text{when } 10^3 < Re < 2 \times 10^5 \quad (5)$$

As shown in Fig. 2, the Nu number obtained by the CFD model agrees reasonably well with the experimental data and the correlation. Quantitatively, the maximum discrepancy between our CFD results relative to the correlation is around +30% for $Re < \sim 1000$ and -30% for $Re > \sim 1000$ (significant transition phenomenon occur near $Re = 1000$). The modeling of heat transfer from cylinder banks is still not completely understood, and the agreement shown in Fig. 2 is within the scatter of existing data [16]. Other parameters and properties used in the calculation of Fig. 2 are found in Table 1.

Inside the batteries, heat conduction was considered only in the radial and azimuthal directions, but not in the axial direction. The rate of heat release (Q) from each battery cell is calculated by:

$$Q = I(t)^2 \cdot R(T) \quad (6)$$

where I represents the charging or discharging current (which can vary with time, t), and R the electrical resistance of each cell (which depends on the cell temperature, T). The following correlation is used to calculate R [21] when T assumes the unit of $^\circ\text{C}$:

$$R = -0.0001 \cdot T^3 + 0.0134 \cdot T^2 - 0.5345 \cdot T + 12.407 (\text{m}\Omega) \quad (7)$$

Note that in this study, the experiments were only conducted under continuous charging or discharging conditions, not under alternating charging and discharging conditions. Therefore, the model only considered the Joule heat as expressed in Eq. (6), and neglected any reversible heat generated due to cycling.

3. Experimental setup

The experimental scheme is shown in Fig. 3, where Panel (a) illustrates the overall experimental facility and Panel (b) describes the configuration of the battery pack and the thermocouples used for temperature measurement. As shown in Panel (a), the battery pack was placed in the test section (with a dimension of $75 \times 75 \text{ cm}$) of an open jet wind tunnel. The wind tunnel is powered by a 30 HP BC-SW Size 365 Twin City centrifugal fan. The fan is

Table 1
Parameters and thermophysical properties used in this work.

Battery properties		Air properties	
Density (kg m^{-3})	$\rho_c = 2007.7$	Density (kg m^{-3})	$\rho_f = 1.1614$
Heat capacity ($\text{J kg}^{-1} \text{K}^{-1}$)	$C_c = 837.4$	Heat capacity ($\text{J kg}^{-1} \text{K}^{-1}$)	$C_f = 1007$
Heat conductivity ($\text{W m}^{-1} \text{K}^{-1}$)	$k_c = 32.2$	Heat conductivity ($\text{W m}^{-1} \text{K}^{-1}$)	$k_f = 0.0263$
Mass per cell (kg)	$M = 0.3$	Dynamic viscosity (Pa s^{-1})	$\mu_f = 1.846 \times 10^{-5}$

capable of providing a maximum volumetric flow rate of $15 \text{ m}^3 \text{ s}^{-1}$ at its maximum fan speed of 1180 RPM. Such maximum volumetric flow rate corresponds to a freestream velocity of $\sim 30 \text{ m s}^{-1}$ in the test section. The fan speed is adjustable and the flow speed is controlled by an AF-600 GE variable frequency drive. Static pressure taps at the exit of the settling chamber measure the freestream velocity.

As shown in Panel (b), the battery module studied in this research consisted of eight lithium ion cylindrical cells (model A123 26650, 2.3 Ah and 3.3 V), which were assembled into a $2\text{P} \times 4\text{S}$ configuration (where P stands for parallel and S stands for series). Under this configuration, the module was rated at 4.6 Ah and 12.8 V with a voltage cut-off limits of 8 V at various C-rates. The size of the eight lithium battery cells is the same: 62.5 mm in height and 25.85 mm in diameter. The height of the battery pack is 65.15 mm, with about 3 mm of space to accommodate electrical and thermocouple wiring. The spacing between two adjacent rows of batteries was 2 mm, and the spacing between two columns was 15 mm. In practical application, it is desirable to minimize such spacing for the consideration of the compactness of the battery pack. However, here the spacing was designed to provide enough space to install the thermocouples. Note that under such spacing, the size of the thermocouple is relatively large, causing disturbance to the flow fields. To overcome such limitations, the integration of an optical temperature sensor is undergoing, so that the temperature can be measured non-intrusively using diode laser absorption spectroscopy [25], or even the 2D temperature distribution can be measured by combining absorption spectroscopy with tomography [26,27]. In the current setup, as shown in Panel (b), five K-type thermocouples (labeled T_1 – T_5) were installed within the battery module at the locations shown. The thermal couples were calibrated before use and the accuracy of these thermal couples was 0.3°C under a room temperature of $\sim 20^\circ\text{C}$.

Other components in the experiment included 1) two protection circuit boards, which were used in the battery module to balance the voltage of each cell during charge/discharge, preventing short circuiting and reversed polarity, 2) a battery analyzer and a charger, which were connected with the module to measure current and voltage *in situ* during tests, 3) two more K-type thermocouples to monitor the room temperature and air flow temperature at the inlet, and 4) a multichannel Data Acquisition (DAQ) card and a

computer to record the data taken during tests. Lastly, note that a pressure rake was also installed to measure the pressure distribution downstream of the battery module for the analysis of aerodynamics of the battery pack. This current paper focuses on the temperature measurements and the heat transfer issues, and the pressure measurements and aerodynamics of the battery pack will be treated in a separate paper.

During the test, the batteries were charged or discharged at different rates and under different air flow velocities ranging from 0 to 5 m s^{-1} (0 m s^{-1} simply corresponded to the case where the wind tunnel was turned off). In each test, the temperatures measured by all thermocouples were recorded every 1 s (the maximum temporal response of the thermocouple is 0.83 ms), and the results are discussed in more details immediately below.

4. Results and discussions

Fig. 4 shows a set of experimental datasets compared with simulations generated by the CFD model described in Section 2. In Fig. 4, the temperatures history at various locations measured under different air velocities are compared to those predicted by the CFD model. This set of data was obtained under 1C discharging (i.e., with a discharging current of 2.3 A). The ambient air temperature was stable at 20.5°C during these tests. The temperature of the air flow at the inlet of the wind tunnel test section increased from 20.5°C to 21.1°C during the first ~ 5 min after the wind tunnel was turned on due to the warming up of the fan engine. After the first ~ 5 min, the temperature of the air flow stabilized within 0.2°C through the tests. Such temperature fluctuation was included in the CFD model via a UDF. Panels (a) and (b) show the temperatures at location T_1 obtained under an air flow velocity of 0 and 5 m s^{-1} , respectively. Panel (c) shows the temperature at location T_4 under an air flow velocity of 5 m s^{-1} .

As can be seen from Fig. 4, the results generated by the CFD model are in reasonable agreement with the experimental datasets, confirming the validity and accuracy of the CFD model. Both the experimental data and CFD simulation show that forced convection at $U = 5 \text{ m s}^{-1}$ is more effective than the natural convection at $U = 0 \text{ m s}^{-1}$ for cooling the batteries. A temperature rise of $\sim 5^\circ\text{C}$ is observed under $U = 0 \text{ m s}^{-1}$ and $\sim 1.5^\circ\text{C}$ under $U = 5 \text{ m s}^{-1}$. However, as the inlet air velocity increases, the pressure drop also

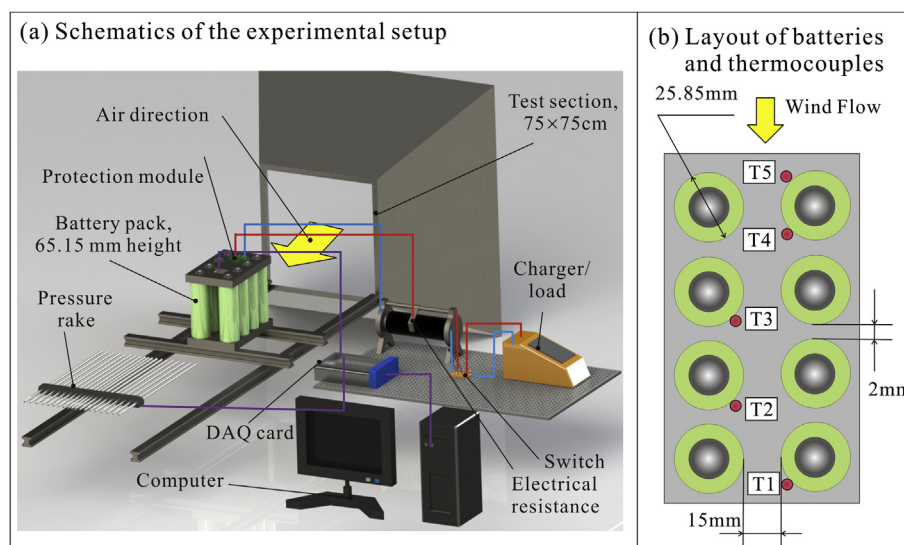


Fig. 3. Illustration of the experimental facilities.

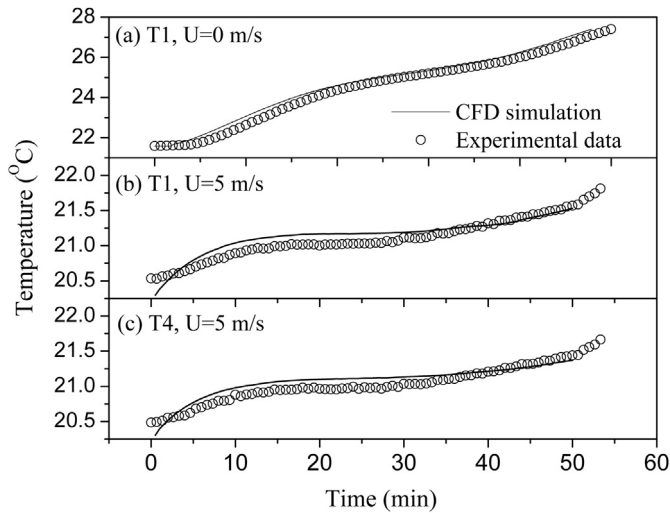


Fig. 4. Comparison between experimental datasets and simulations from the CFD model. Panel (a). Temperature at location T_1 under $U = 0 \text{ m s}^{-1}$. Panel (b). Temperature at location T_1 under $U = 5 \text{ m s}^{-1}$. Panel (c). Temperature at location T_4 under $U = 5 \text{ m s}^{-1}$.

increases, leading to higher pumping power requirement. As mentioned in Section 3, we are using a pressure rake to measure the pressure distribution, and the measurements are being analyzed to quantify the pressure drop.

These results also show some disagreements between the experimental datasets and the CFD simulations. As shown in Panels (b) and (c), the temperature during the first 10 min does not agree well under $U = 5 \text{ m s}^{-1}$. Our possible explanations for such disagreement include:

- 1) As mentioned earlier, the wind was warmed up during the first 5 min so that the incoming air flow's temperature increased by about 0.6°C . Such effects may not be properly treated in our current model. This explanation is supported by the better agreement shown in Panel (a) under $U = 0 \text{ m s}^{-1}$, where the test did not involve the wind tunnel. For future work, we will improve the UDFs to model the fluctuation in the inlet air temperature, and start testing 10 min after the wind tunnel is turned on.
- 2) As mentioned in Section 3, the thermocouples have an accuracy of 0.3°C and their intrusiveness cannot be neglected due to their relative large size compared to the spacing among the batteries. As shown in Fig. 4, the magnitude in temperature rise decreases as inlet air velocity increases, making the effects of the thermocouples' accuracy and intrusiveness increasingly more significantly with increasing inlet air velocity. For future work, we are developing non-intrusive temperature sensors based on diode laser absorption spectroscopy to address these issues.

With the above validation and understanding of the CFD model, it can be applied to study effects which are of interests in practice but hard to study experimentally. Such examples include the effects of battery operation under extreme temperatures and humidity, and temperature non-uniformity among cells. Fig. 5 shows the temperature non-uniformity simulated by the CFD model under two representative inlet air velocities $U = 5 \text{ m s}^{-1}$ (Panel a) and $U = 1 \text{ m s}^{-1}$ (Panel b) in a battery pack consisting of 32 cells, as configured according to Section 2. The batteries are assumed to be 100% charged initially and start discharging at 10C (25.2 A). Under these configurations, the volumetric air flow rates are, respectively,

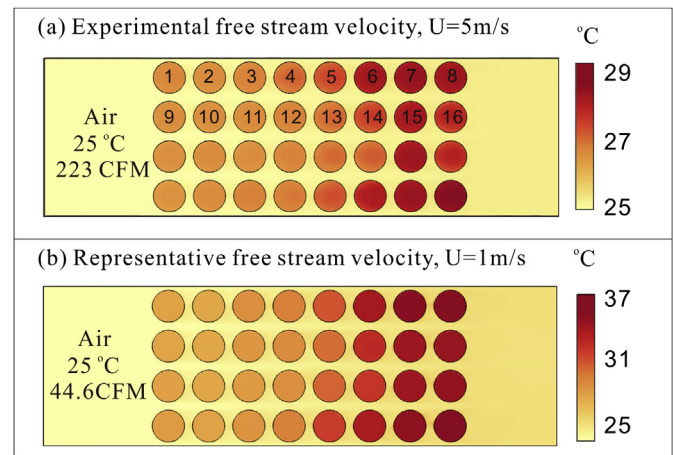


Fig. 5. Temperature non-uniformity simulated by the CFD model under two representative inlet air velocities: Panel (a). $U = 5 \text{ m s}^{-1}$ and Panel (b). $U = 1 \text{ m s}^{-1}$ case.

223 and 44.6 CFM (cubic feet per minute). The simulation was performed assuming that the temperature of the ambient air and the cooling air is stable at 25°C . The initial temperature of the cells is also assumed to be 25°C .

Significant temperature non-uniformity can be observed from these results. Batteries near the inlet of cooling air have lower temperature than batteries near the outlet, which is intuitive because the cooling air is being heated gradually as it passes the battery cells. Under $U = 5 \text{ m s}^{-1}$, the highest battery temperature is $\sim 28.6^\circ\text{C}$ (a temperature rise of 3.6°C). Under $U = 1 \text{ m s}^{-1}$, the highest battery temperature is $\sim 37.0^\circ\text{C}$ (a temperature rise of 12°C).

Fig. 6 further illustrates the temperature rise and the temperature non-uniformity. Here, the maximum temperature on each cell for cells 1–16 (as denoted in Fig. 5) is shown. These results clearly show the trend of increasing cell temperature and temperature non-uniformity as the cooling air flows downstream. For instance, under $U = 5 \text{ m s}^{-1}$, the eighth cell's temperature is higher than the first one by $\sim 0.5^\circ\text{C}$; and under $U = 1 \text{ m s}^{-1}$, the eighth cell's temperature is higher than the first one by $\sim 3.5^\circ\text{C}$. Also, the highest cell temperature occurred at the seventh row and/or the eighth row (as shown in these results), which is an observation that valuable for the development of the reduced-order model to be described in Section 5. Furthermore, Fig. 6 indicates that the cells next to the wall (cells 1–8) have higher temperature than cells in the central area (cells 9–16) both because of the insulating wall assumption made here and because of the boundary layer effects near the wall.

To summarize, a CFD model has been developed and validated by experimental datasets. The CFD model was then applied to study the temperature non-uniformity among cells in a battery pack. The CFD model and experimental datasets are expected to be useful for the design of battery cooling system. The observations made from the CFD results and experimental datasets also suggest the development of a reduced-order model, as described in the section immediately below.

5. Reduced-order model

In a simplest reduced-order model (named a one-zone model here), all the battery cells can be considered to have the same temperature as in the analysis of overall performance of tube-bank heat exchangers [24]. However, as discussed in Section 4, there are significant temperature non-uniformities among cells in a pack and

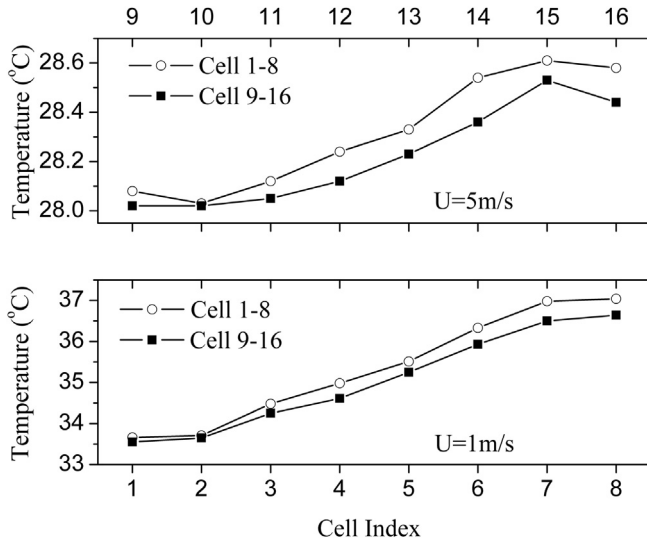


Fig. 6. Temperature non-uniformity among different cells in the battery pack at steady state. Panel (a). $U = 5 \text{ m s}^{-1}$ case. Panel (b). $U = 1 \text{ m s}^{-1}$ case.

the hot spots in the pack are of particular interests. Therefore, such a one-zone model is not suitable and a simple model is desired to predict the maximum temperature in the pack. This section describes a two-zone model for this purpose.

The two-zone model is based on the observation made from the results shown in Section 4. As Figs. 5 and 6 indicate, the highest temperature occurs in the rows that are nearest to the outlet, i.e., the seventh and eighth rows in the cases of Figs. 5 and 6. Therefore, a reduced-order model is developed, as shown in Fig. 7, to divide the battery pack into two zones. The second zone includes the last two rows of battery cells, and all the cells in this zone are assumed to have the same temperature (T_{\max}). The rest of the rows of batteries are included in the first zone, whose temperature is assumed to be uniformly T_S . The cooling air will first flow through the first zone, and the air exiting the first zone (at a temperature of T_{mid}) will enter the second zone and provide cooling to the cells in this zone. The air finally exits the second zone at a temperature of $T_{f,o}$.

Since each zone is assumed to have a uniform temperature, all the cells in each zone can be analyzed in a lumped fashion as detailed in Ref. [24]. Take zone one for example, the analysis will be performed in the following steps. First, the log-mean temperature difference (T_{LMTD}) is calculated by:

$$T_{\text{LMTD}} = \frac{(T_S - T_{\text{mid}}) - (T_S - T_{f,i})}{\ln\left(\frac{T_S - T_{\text{mid}}}{T_S - T_{f,i}}\right)} \text{ and } \frac{T_S - T_{\text{mid}}}{T_S - T_{f,i}} = \exp\left(-\frac{\pi D n h}{\rho_f U S_T C_f}\right) \quad (8)$$

Here, h is calculated using Eq. (3), with the Nu number obtained from the correlation in Ref. [23] as shown in Eq. (5). There are three unknowns (T_{mid} , T_S , and T_{LMTD}) in these two equations. As such, one more equation is needed and this equation is provided by Eq. (9) below:

$$Q = h\pi DHT_{\text{LMTD}} = I^2 R(T_S) \quad (9)$$

Eq. (9) is derived by applying the conservation of energy to zone one under steady state, where the heat transferred out of zone one is balanced by the heat generation by the batteries. Note that 1) in our current model, the current, I , is a constant that does not vary with time, and 2) the electric resistance, R , is dependent on the

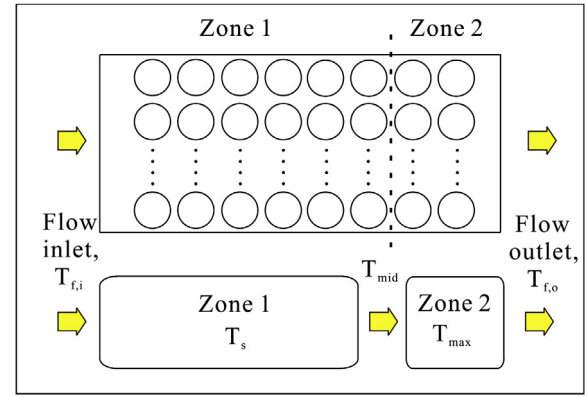


Fig. 7. Schematics of the two-zone reduced-order model.

temperature of the first zone (T_S). This current model is being extended to incorporate unsteady charging and discharging currents. Solving the three equations in Eqs. (8) and (9) yields T_{mid} , T_S , and T_{LMTD} . Then T_{mid} is used as the inlet temperature for the second zone, and similar calculations as described in Eqs. (8) and (9) are performed to obtain T_{\max} and $T_{f,o}$ of the second zone.

Fig. 8 compares the T_{\max} obtained from the above two zones against those calculated by the high-fidelity CFD described in Section 2 for a case with eight rows of cells. These results were obtained under the same configurations as those used in Figs. 5 and 6. For the CFD results, the highest and lowest cell temperature were plotted to show the range of temperature variation among cells. The comparison was made under various freestream velocities ranging from 0.2 to 10 m s^{-1} , corresponding to a Re range of 2660 to 133,000, encompassing the range of practical interests. Panel (a) of Fig. 8 shows the comparison of T_{\max} from the two zone model compared to the CFD results, and Panel (b) shows the difference between T_{\max} obtained from the two-zone model versus the maximum cell temperature obtained from the CFD model.

Satisfactory agreement is observed from Fig. 8 between the reduced-order model and the CFD model in terms of the maximum temperature. The two-zone model accurately captures the reduction of the maximum temperature as freestream velocity increases, which suggests its usefulness for predicting the maximum temperature in the battery packing. The computation cost involved in the two-zone model is negligible, making it promising for *in situ* analysis and active control purposes. Panel (b) shows that the two-zone model overestimated the maximum temperature at $Re = 2660$ ($U = 0.2 \text{ m s}^{-1}$) by $\sim 3^\circ\text{C}$ and underestimated for other Re numbers. The agreement between the reduced-model and the CFD model improves with increasing Re number, though this is mainly caused by the fact that the temperature of the cells in the battery pack becomes increasingly more uniform (which approaches the inlet air temperature) as the Re number increases. Our explanation for the underestimation by the two-zone model for at large Re numbers is that the CFD predicts a lower h comparing to the correlation used in the two-zone model, as shown in Fig. 2. The CFD model predicts lower h , resulting in less efficient heat transfer and therefore higher cell temperature.

Fig. 9 shows the temperature of the cooling air at the exit of the battery pack predicted by the two-zone model and the CFD model. Panel (a) compares the exit temperatures, and Panel (b) shows the difference between these exit temperatures. As can be seen, the temperature difference is generally less than $\pm 1^\circ\text{C}$ except at the lowest Re number simulated ($Re = 2660$). Our explanation for the large disagreement at $Re = 2660$ is that the disagreement between the h predicted by the CFD model and that by the Zukauskas

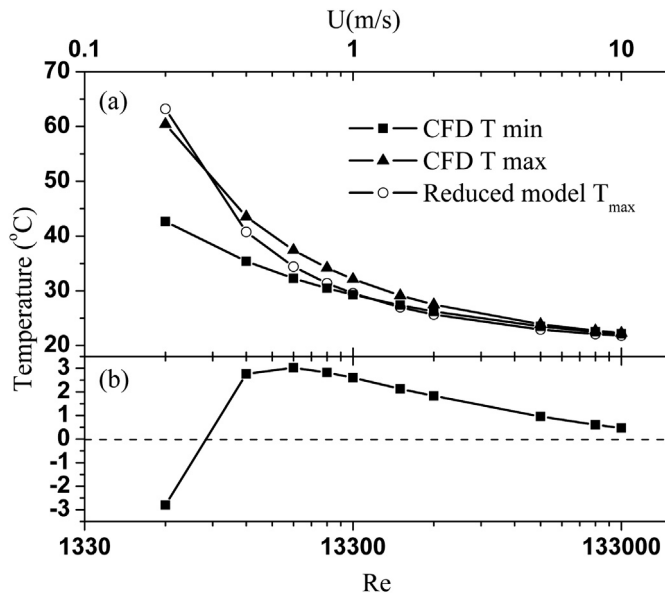


Fig. 8. Comparison of the maximum cell temperature predicted by the two zone model and the CFD model under different Re numbers. Panel (a) shows the T_{\max} predicted by the two-zone model, and the maximum and minimum temperatures predicted by the CFD model. Panel (b) shows the discrepancy of the maximum cell temperature obtained from the two-zone and the CFD model.

correlation is large near the transition regime (especially in Re range 1000–2000) as shown in Fig. 2. These results further confirm the validity and accuracy of the reduced-order model. Moreover, the exit temperature of the cooling air is an important parameter for the design of the cooling loop.

In summary, a simple two-zone model is developed. The model has been demonstrated to predict the maximum cell temperature and exit temperature of the cooling air with reasonable accuracy in a wide range of Re number when compared to the high-fidelity CFD model.

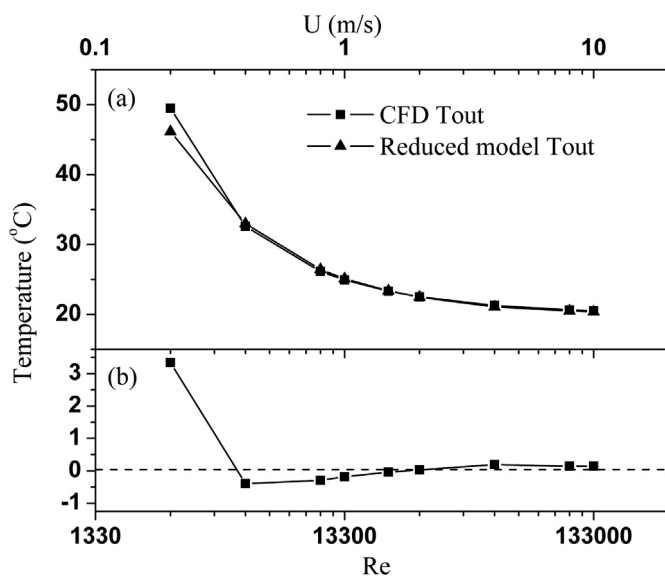


Fig. 9. Comparison of the flow outlet temperature predicted by the two-zone model and the CFD model under different Re numbers. Panel (a) shows the T_{out} predicted by the two-zone model and the CFD model. Panel (b) shows the discrepancy of the maximum outlet flow temperature obtained from the two-zone and the CFD model.

6. Summary

In summary, this work studied thermal management of lithium ion batteries both numerically and experimentally under the context of electric vehicles and hybrid electric vehicles. A high-fidelity CFD model was developed to perform detailed simulations of the cooling of battery packs. The model results were directly compared to experimental data and reasonable agreement were observed. Possible reasons for the discrepancy were discussed, and approaches to improve both the modeling and experimental efforts were described (summarized in the following paragraph). With an understanding of the CFD model's accuracy and validity confirmed by experimental datasets, the CFD model was applied to study the temperature distribution within a battery pack, revealing significant temperature non-uniformity. Observations obtained from the non-uniform temperature distributions suggested the development of a reduced-order model to capture the extreme temperature in the pack. A two-zone model was then developed, and showed good accuracy for predicting the maximum temperature in the pack. Because of its simplicity and accuracy, the two-zone model is expected to be useful for *in situ* analysis and active control purposes.

Ongoing experimental work is concentrated in three areas. First, we are analyzing the pressure measurements to study the aerodynamics of the battery pack and the drag produced by the pack, which is directly related to the power required to drive the cooling air through the battery pack. Second, we are using the experimental facility to test battery packs with various geometrical configurations and battery types. Such tests will be combined with the reduced-order model and high-fidelity CFD model to optimize the design of the battery packing and operation. Third, we are developing an optical temperature sensor for integration in the experimental facility, so that temperature [25] or even 2D temperature distribution [26,27] can be measured non-intrusively based on tunable diode absorption spectroscopy. Ongoing modeling efforts are concentrated in two areas. First, we are testing various turbulence and battery sub-models. Second, we are extending the two-zone reduced-model to analyze dynamic charging and discharging of the battery pack.

Acknowledgment

The authors gratefully acknowledge the support provided by the Automotive Research Center (ARC), a U.S. Army Center of Excellence in Modeling and Simulation of Ground Vehicles.

References

- [1] D. Linden, T. Reddy, Handbook of Batteries, third ed., McGraw-Hill, New York, 2001.
- [2] H. Joachin, T. Kaunb, K. Zaghib, J. Prakash, Journal of the Electrochemical Society 6 (2008) 11–16.
- [3] Electric and Hybrid Vehicles, first ed., Elsevier, Oxford, UK, 2010.
- [4] J. Siegel, X. Lin, A. Stefanopoulou, in: American Control Conference, Fairmont Queen Elizabeth, Montréal, Canada, 2012.
- [5] J. Siegel, X. Lin, A. Stefanopoulou, D.S. Hussey, D.L. Jacobson, D. Gorsich, Journal of the Electrochemical Society 158 (2011) A523–A529.
- [6] D. Di Domenico, A. Stefanopoulou, G. Fiengo, Journal of Dynamic Systems, Measurement, and Control 132 (2010).
- [7] C. Pals, J. Newman, Journal of the Electrochemical Society 142 (1995) 3274–3281.
- [8] M. Doyle, J. Newman, A. Gozdz, C. Schmutz, J. Tarascon, Journal of the Electrochemical Society 143 (1996) 1890–1903.
- [9] T. Hatchard, D. MacNeil, A. Basu, J. Dahn, Journal of the Electrochemical Society 148 (2001) A755–A761.
- [10] J. Newman, W. Tiedemann, Journal of the Electrochemical Society 142 (1995) 1054–1057.
- [11] D. Jeon, S. Baek, Energy Conversion and Management 52 (2011) 2973–2981.
- [12] K. Yeow, H. Teng, M. Thelliez, E. Tan, 2012 SIMULIA Community Conference, 2012.

- [13] C. Pals, J. Newman, *Journal of the Electrochemical Society* 142 (1995) 3282–3288.
- [14] H. Sun, X. Wang, B. Tossan, R. Dixon, *Journal of Power Sources* 206 (2012) 349–356.
- [15] C. Zhu, X. Li, L. Song, L. Xiang, *Journal of Power Sources* 223 (2013) 155–164.
- [16] R. Mahamud, C. Park, *Journal of Power Sources* 196 (2011) 5685–5696.
- [17] X. Duan, G. Naterer, *International Journal of Heat and Mass Transfer* 53 (2010) 5176–5182.
- [18] G. Kim, J. Gonder, J. Lustbader, A. Pesaran, *The World Electric Vehicle Journal* 2 (2008).
- [19] S. Khateeb, S. Amiruddin, M. Farid, J. Selman, S. Al-Hallaj, *Journal of Power Sources* 142 (2005) 345–353.
- [20] A. Taha, D. Ewing, Y. Zhao, L. Ma, *SAE International Journal of Materials and Manufacturing* 2 (2009) 85–91.
- [21] C. Park, A. Jaura, *SAE Technical Paper* (2003), 2003-2001-2286.
- [22] F. He, D. Ewing, J. Finn, J. Wagner, L. Ma, *SAE Technical Paper* (2013), 2013-01-1641.
- [23] A. Zukauskas, R. Ulinskas, *Heat Transfer in Tube Banks in Crossflow*, Springer-Verlag, New York, 1988.
- [24] F. Incropera, D. Dewitt, *Fundamentals of Heat and Mass Transfer*, fourth ed., John Wiley & Sons, New York, 1996.
- [25] X. Sun, D. Ewing, L. Ma, *Particuology* 10 (2012) 9–16.
- [26] L. Ma, X. Li, S. Sanders, A. Caswell, S. Roy, D. Plemmons, J. Gord, *Optics Express* 21 (2013) 1152–1162.
- [27] X. An, T. Kraetschmer, K. Takami, S. Sanders, L. Ma, W. Cai, X. Li, S. Roy, J. Gord, *Applied Optics* 50 (2011) A29–A37.